

---

# AN APPROACH TO SIMULATE FLUID STRUCTURE INTERACTION INVOLVING FREE SURFACE FLOWS

Vom Fachbereich Maschinenbau  
an der Technischen Universität Darmstadt  
zur Erlangung des Grades eines  
Doktor-Ingenieurs (Dr.-Ing.)  
eingereichte

## **Dissertation**

vorgelegt von

**Dipl.-Ing. Jessica Marcela Mariño Salguero**

aus Ecuador

Berichterstatter: Prof. Dr. rer. nat. Michael Schäfer

Mitberichterstatter: Prof. Dr.-Ing. #####

Tag der Einreichung: ##.##.2020

Tag der mündlichen Prüfung: ##.##.2020

Darmstadt 2020

D 17

---

## Abstract

Simulating the interaction of multiphase flows with rigid or flexible structures is of great interest for enhancing the design of marine structures. Another problem is the dependence on a low Courant number to accurately capture the fluid interface, resulting in excessively long computational times. This work overcomes the mentioned problems with a new efficient, and stable implicit partitioned fluid-structure interaction (FSI) approach where the fluid calculation is performed with the in-house solver FASTEST, using a finite volume method. In contrast, the structural calculation is solved with the CALCULIX program, based on the finite element method. The two solvers are coupled via the PRECICE multiphysics platform. In each time step, the solvers act iteratively, serially or in parallel, the fluid solver receives displacements and sends forces, while the structural solver receives forces and send displacements. The coupling is stabilized and accelerated with quasi-Newton methods, filters, and extrapolation.

The multiphase dynamics are described with the one-fluid formulation of the Navier-Stokes equations and the volume fraction transport equation in the arbitrary Lagrangian-Eulerian (ALE) framework to deal with the moving domain. The fluid interface is captured with an algebraic volume of fluid (VOF) method based on high-resolution schemes implemented through a new modified normalized weighting factor (MNWF) technique that maintains fluid interface sharpness and stability for high Courant numbers ( $Co > 1$ ). Consequently, FSI simulations can use large time-steps and thus reduce the computational time. Also, dynamic switching between SIMPLE and PIMPLE is applied to achieve high convergence of the pressure-velocity coupling. The new approach is validated considering a dam break with an elastic obstruction as a test case. The simulation results are in accordance with the literature references, and the method shows a positive effect on accuracy, computational time and stability.

---

## ACKNOWLEDGEMENTS

This work is supported by the “Excellence Initiative” of the German Federal and State Governments within the Graduate School of Computational Engineering at Technische Universität Darmstadt.

## CONTENTS

<b>1.</b>	<b>INTRODUCTION .....</b>	<b>5</b>
1.1.	INTRODUCTION AND MOTIVATION .....	5
1.2.	STATE OF THE ART .....	6
1.2.1.	<i>Numerical Methods to solve free-surface flows .....</i>	<i>6</i>
1.2.2.	<i>Interface Tracking Methods (ITM) .....</i>	<i>8</i>
1.2.3.	<i>Meshless methods .....</i>	<i>9</i>
1.3.	NUMERICAL METHODS FOR TRACKING FLUID-STRUCTURE INTERFACE .....	9
1.3.1.	<i>Immersed boundary methods .....</i>	<i>9</i>
1.4.	NUMERICAL METHODS FOR MODELING FLUID-STRUCTURE INTERACTION (FSI) PROBLEMS .....	9
1.5.	FLUID-STRUCTURE INTERACTION INVOLVING FREE SURFACE FLOWS .....	10
1.6.	SCOPE AND OBJECTIVES .....	10
1.7.	OUTLINE .....	10
<b>2.</b>	<b>MATHEMATICAL MODELING OF THE PHYSICAL PHENOMENA .....</b>	<b>11</b>
2.1.	THE PROBLEM DEFINITION AND MODELING APPROACHES .....	11
2.2.	TWO-FLUID FLOW DOMAIN .....	12
2.3.	ELASTIC STRUCTURAL DOMAIN .....	13
2.3.1.	<i>Kinematics .....</i>	<i>Error! Bookmark not defined.</i>
2.3.2.	<i>Balance law .....</i>	<i>Error! Bookmark not defined.</i>
2.3.3.	<i>Constitutive law .....</i>	<i>Error! Bookmark not defined.</i>
2.4.	INTERACTION CONDITIONS .....	15
<b>3.</b>	<b>DISCRETIZATION OF THE FLUID DOMAIN .....</b>	<b>16</b>
3.1.1.	<i>Spatial discretization of the fluid domain .....</i>	<i>16</i>
3.1.2.	<i>Discretization of the equations .....</i>	<i>18</i>
3.1.3.	<i>Discretization of the momentum equation .....</i>	<i>19</i>
3.1.4.	<i>Green Gauss gradient with the midpoint correction for non-orthogonal grids .....</i>	<i>21</i>
3.1.5.	<i>Face values of density and viscosity .....</i>	<i>22</i>
3.1.6.	<i>Treatment of the Body Force Term .....</i>	<i>23</i>
3.1.7.	<i>Convective term .....</i>	<i>25</i>
3.1.8.	<i>Set of linear equations .....</i>	<i>25</i>
3.1.9.	<i>Equilibrium condition and discretization of volume forces .....</i>	<i>25</i>
3.1.10.	<i>Boundary conditions .....</i>	<i>25</i>
3.1.11.	<i>Pressure and velocity coupling .....</i>	<i>25</i>
3.2.	DISCRETIZATION OF THE VOLUME-FRACTION TRANSPORT EQUATION .....	26
3.2.1.	<i>Temporal discretization .....</i>	<i>26</i>
3.2.2.	<i>Spatial discretization .....</i>	<i>26</i>
3.2.3.	<i>Normalized variable diagram and high-resolution schemes .....</i>	<i>26</i>
3.2.4.	<i>Normalized variables on non-uniform and unstructured mesh .....</i>	<i>26</i>
3.2.5.	<i>Compressive high-resolution schemes .....</i>	<i>26</i>
3.2.6.	<i>Discretization of surface tension term .....</i>	<i>26</i>
3.2.7.	<i>Comparison of high-resolution compressive schemes .....</i>	<i>26</i>
<b>4.</b>	<b>RESULTS .....</b>	<b>27</b>
4.1.	CODE VERIFICATION OF THE PRESSURE-VELOCITY COUPLING ALGORITHM .....	27

---

4.2.	VALIDATION OF THE FLUID-STRUCTURE INTERACTION COUPLING .....	30
------	--	----

List of Figures

List of Tables

Notation and Nomenclature

---

## 1. INTRODUCTION

---

### 1.1. Introduction and motivation

Fluid-structure interaction (FSI) involving free-surface flows is a transitory and nonlinear multi-physical phenomenon. On the one hand, fluid-structure interaction refers to the physical phenomenon produced when a flow induces compression and shear forces on the surface of a structure which moves or deforms the structure. The structural position changes affect the dynamics of the surrounding flow, which changes the compression and shear forces on the structure. It results in a continuous process where each flow adaptation also induces an adaptation of the structure position. The physical coupling of the fluid field and structural field is mathematically modeled as a dynamic equilibrium at the fluid-structure interface.

According to Naudascher & Rockwell (Naudascher & Rockwell, 2012), in a fluid-structure interaction situation, two basic elements exist the oscillators and a source of excitation. Oscillators are structural or fluid mass systems that restore forces if they deviate from their equilibrium positions. A structural oscillator can be a rigid structure that is elastically supported, or an elastic structure because they can perform flexural movements. The fluid oscillator is a passive mass of fluid that may undergo oscillations due to the compressibility of the fluid or by gravity. A fluid oscillator can cause undesirable fluid pulsations when excited (e.g. rogue waves); and can amplify the vibration of a structural oscillator if one of its natural frequencies matches the natural frequency of the structural oscillator.

The sources of excitation are classified into three types: extraneously induced excitation, instability-induced excitation, and movement induced excitation. The extraneously induced excitation is caused by fluctuations in flow velocities or pressures that are independent of any flow instability originated by the structure and independent of structural movements. An example is a cylinder being hit by the turbulence of the incoming flow. By contrast, the instability-induced excitation is produced through a flow process (or flow instabilities). This instability is inherent to the flow created by the structure considered. An example of this situation is presented in the FSI test case of Turek and Hron (Stefan Turek & Hron, 2006). The oscillation of an elastic beam caused by the alternating vortex shedding from an upstream cylindrical structure. Whereas, the movement-induced excitation is due to fluctuating forces arising from the movements of the structural oscillator or flow oscillator. The vibrations of the latter are self-excited. For example, if a hydrofoil receives an adequate disturbance, the flow will induce a pressure field that tends to increase that disturbance. The energy transferred from the flow to the structure results in dynamic instability of the structural oscillator.

On the other hand, free-surface flows are a special case of the multiphase flow systems. Regularly this implies the two-phase flow system form by air-water.

The fluid-structure interaction (FSI) involving free-surface flows plays a dominant effect in the design and operation of many engineering systems, especially in the field of naval architecture, civil engineering, and marine engineering. Since marine structures such as ships and offshore structures are massive and capital-intensive structures placed in an unfriendly environment where the green water effect produced by regular and giant waves can damage them. The wave overturning, breaking and collapse during the initial stage of green water phenomena results in high-frequency vibration of the deck structure that produces damages by fatigue. Additionally, the dropping impact induced by the vast water volume that falls onto the deck can lead to a relatively large structure deformation (Hu, Tang, Xue, Zhang, & Wang, 2017). Consequently, research to better comprehends the interaction of structures with free surface flows, skilled engineers, and efficient design tools are required in order to enhance and optimize the designs of marine structures and prevent damage.

Because this multi-physical phenomenon has no analytical solutions for the most part and laboratory experiments are difficult and expensive to perform. The numerical simulations seem to be

---

a better choice to obtain valuable information about the phenomena with less effort. In the last three decades, several numerical methods have been developed that partially solve the problem. Intensive investigations have focused on creating numerical models that accurately describe the dynamics of free surface water flow around moving rigid bodies. For example, the doctoral works by Fekken (Fekken, 2004) presents a simulation model for studies of floating ship-type, interacting in waves with or without impact phenomena. The water entry of wedge-shaped geometries was also investigated. A good summary of the methods currently applied for ship hydrodynamics is given by (Wackers et al., 2011), and other examples the reader can find in (Akkerman, Bazilevs, Benson, Farthing, & Kees, 2012; Pin, Idelsohn, Oñate, & Aubry, 2007). They have reached their maturity in development. They are now commonly used to solve real industrial applications. For example, in the shipping industry, numerical simulation of flow around a rigid ship moving at a certain speed is used in the design stage to estimate the hydrodynamic resistance of the ship and then minimize it by proper hull-shape design (Wackers et al., 2011). Also, researchers are using these methods to explore alternatives to propeller propulsion, such as fin propulsion (Pedersen, 2015).

On the other hand, the consideration of the structure as a rigid body does not apply to the design of the new generation of large containers. Ultra-large container ships have large open deck areas and thereby highly nonlinear wave-induced loading, so hull flexibility plays an essential role in the response of the vessel. For these ships, the hull-beam vibration natural frequencies become as low as 0.40 Hz. They can be continually excited due to the high-frequency components in the wave spectrum and to nonlinear excitation effects. So, to calculate the wave-induced load and prevent fatigue damage to the hull, the flexibility of the structure must be considered. Similarly, for offshore structures used for the extraction of hydrocarbons and minerals below the seabed at great water depths or in arctic waters, as well as for sustainable energy production, the flexibility of these floating platforms and their support elements are an important parameter to properly estimate fatigue damages and prevent direct resonance with dominant ocean wave frequencies (Pedersen, 2015). Therefore, the development of consistent, efficient, and stable numerical methods is required to calculate the interaction between waves and elastic structures.

Another critical point is the improvement of hydrodynamic calculation procedures involving flow around the slender bodies which is essential for the development of offshore wind turbines.

However, the numerical methods that describe the interaction between free-surface flows and elastic structure when the deformation is not neglected is still a challenge. Because the two fields describing multiphase fluid dynamics and structural dynamics must be carefully coupled to overcome the instability and decoupling caused by abruptly changing load conditions at the fluid-structure interface which result from the large density differences within the flow domain (Bogaers, Kok, Reddy, & Franz, 2016).

## **1.2. State of the art**

### **1.2.1. Numerical Methods to solve free-surface flows**

The last decades, several different methods for computations of multiphase flows problems have been developed and improved. In this section, I will give a brief overview of the significant efforts to simulate free-surface flows.

In the sixties, Harlow and From (Harlow & Welch, 1965) presented the numerical solution of the so-called dam breaking problem using a new approach, the marker-and-cell (MAC) method, opening up the possibility for simulating real free surface flows. In the MAC method, marker particles define the fluid region, and the governing equations solve the fluid region and the empty part of the domain. Initially, the MAC method assumed a free surface flow, so the method involved only one fluid constrained by proper boundary conditions. However, solving other cases as the Rayleigh-Taylor

---

stability (Harlow & Welch, 1966), and the splash of a droplet onto a liquid surface (Harlow & Shannon, 1967), the Los Alamos group realized that the same methodology could be applied for two-fluid problems. The following years, the MAC method grew in popularity and was used to study several problems. For example, the two-fluid Rayleigh-Taylor instability at different density ratios (Daly, 1967), the run-up of a solitary wave on a vertical wall (Chan & Street, 1970), or the transient dynamics of free surface flows in the vicinity of submerged and penetrate obstacles (Nichols & Hirt, 1973). However, the marker particles sometimes caused inaccuracies and the Los Alamos group, in order to overcome them, replaced the particles by a marker function. Thus, the volume-of-fluid (VOF) of Hirt and Nichols (Hirt & Nichols, 1981) was born and was the begin for the next generation of methods for multifluid flows.

In the VOF method, a discontinuous marker function, the volume fraction of one of the fluids, defines the spatial distribution of the fluids. The volume fraction takes values between zero and one where one denotes presence, zero denotes absence of the traced fluid, and values between zero and one indicate a mixture. The value of 0.5 defines the flow interface. The inherent conservation of mass and the applicability to both structure and unstructured grids makes the VOF method very attractive. However, the volume fraction must be advanced with the flow which, being a discontinuous function, generates numerical diffusion. To prevent the marker function from diffusing, the interface is reconstructed in a manner that the marker does not flow into a new cell until the current cell is full. In the initial implementation of VOF, the interface was considered a vertical plane for advection in the horizontal direction and horizontal for the vertical direction. This assumption often led to a large amount of small unphysical droplets that break away from the interface that degraded the accuracy of the computation (Tryggvason, Scardovelli, & Zaleski, 2001).

To improve the representation of the interface, in the 1980s, several other, more complex geometrically reconstruction approaches were introduced. A comprehensive review of these methods is given in (Rider & Kothe, 1998). The most used approaches are PLIC (for Piecewise Linear Interface Calculation) (Lötstedt, 1982) and SLIC (for Simple Line Interface Calculation) (Ashgriz & Poo, 1991). They accurately approximate the shape of the interface, but are limited for structured grid discretization and requires substantial computational effort (Zaleski, 1996). Later in the 1990s, Davis (Davis, 1994) introduced a more practical approach. Algebraic reconstruction of the interface that ensures a monotonic change of the volume fraction (boundedness) and reduces the numerical diffusion and dispersion near the interface. It combines a less diffusive scheme, that reduces the smearing of the profile, and a compressive scheme, which removes any diffusion near the interface. The blending strategy considers the angle between the flow direction and the grid lines. This concept is until now the basis to develop several blending advection schemes, also known as interface-capture schemes, for example, CICSAM (Ubbink & Issa, 1999), HRIC (Muzaferija & Peric, 1998), IGDS (Jasak, Weller, & Gosman, 1999), STACS (Darwish & Moukalled, 2006), BICS (Queutey & Visonneau, 2007), FBICS (Tsui, Lin, Cheng, & Wu, 2009), CUIBS (Patel & Natarajan, 2015) and others.

VOF methods are extensive use today due to its robustness to handle most of the complex interfaces and free-surface flows. In commercial codes for naval hydrodynamics, for example, VOF is included to track overturning, breaking waves and splashing (Wackers et al., 2011).

The basic idea of the MAC and VOF methods gave rise to other approaches called front-tracking methods. The most known of this group is the level-set (LS) method introduced by (Osher & Sethian, 1988) an Eulerian numerical technique to capture moving interfaces and shapes, where a continuous level-set function is used. The level-set function is defined as a signed normal distance function (Sharma, 2015). The interface is the zero-level set function, and the sign of the function changes across the interface. A marker function is built from the level-set function to track the interface. The marker function has a smooth transition zone from one fluid to the another, thus producing a superior definition of the interface than the VOF method. However, this mapping from the level-set function to

the marker function requires maintaining a constant shape of the level set function near the interface. To address this problem a reinitialization procedure (Sussman, Smereka, & Osher, 1994) needs to be applied in which the level-set function is always adjusted so that its value equals to the shortest distance to the interface. This reinitialization is commonly believed to be the primary source of the weak mass conservation of the method (Bai, Avital, Munjiza, & Williams, 2014).

The sharp interface definition and the ability to model changes in free surface topology have been motivated to find ways to improve the mass conservation of the method. Some technique is combining LS with VOF considering the VOF function when the interface is advected (Ménard, Tanguy, & Berlemont, 2007; Sussman & Puckett, 2000; van der Pijl, Segal, Vuik, & Wesseling, 2005), or coupling the standard LS and the conservative LS method (Zhao, Bai, Li, & Williams, 2014). A detailed list of more techniques can be found in (Sharma, 2015).

In the field of water-air problems, the most used level set method is the single-phase approach, since the single-phase approach only computes the water region, and the air region is extrapolated using the free surface boundary condition (Hino, 2006) resulting in less computational time.

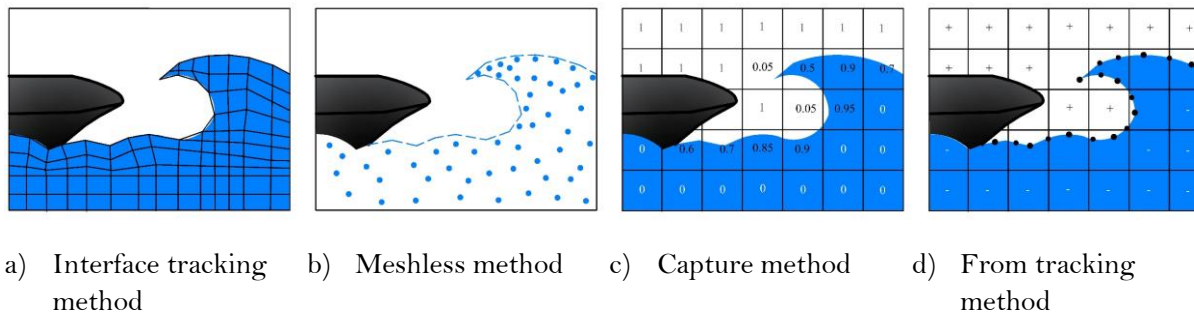


Fig. 1 Techniques to solve the free-surface flow

### 1.2.2. Interface Tracking Methods (ITM)

In the interface tracking methods, the grid is constantly regenerated to fit each current free surface shape. A technic in this group is the Arbitrary Lagrangian-Eulerian (ALE) method. The free surface is approximated as a mesh boundary that moves influenced by the flow. The pressure of the air is assumed constant, and the viscous stresses in the air are negligible. Then, the jump conditions (no phase-change, no-slip at the interface, and force balance) of the interface become a boundary condition for the liquid domain (Tryggvason et al., 2001).

An advantage of the fitting methods is that the form and location of the free surface are explicitly known, and it is always sharp. Thus, more details of the flow near the wave surface are known, and the accuracy of force computation increases (Hoekstra, 1998). The ALE method is very suitable for simulating free-surface problems with large deformation of the interface, but no topological changes are present (Wall, Genkinger, & Ramm, 2007). The method has difficulty in addressing topology changes generated by breaking waves, overturning, or splashing. The strong deformation or topological changes of the interface lead to a degeneration of the computational mesh, and the remeshing techniques are also an additional source of errors. For this reason, in industrial applications, it is usually applied for prediction of steady flow around ship hulls or flows with mild breaking only (Wackers et al., 2011).



---

### 1.2.3. Meshless methods

Particles are used to track the movement of the interfaces. The grid that they form may be adapted to account for any changes in the interfacial shape (Unverdi & Tryggvason, 1992). A successfully approaches are the Smooth Particle Hydrodynamics (SPH) method originally developed in (Gingold & Monaghan, 1977) or the Moving Particle Semi-Implicit Method (MPS) (Koshizuka & Oka, 1996). The SPH method represents the fluid by large particles of fluid which are subject to Newton's Second Law. The spatial derivatives are estimated by analytical expressions and do not need a fixed computation grid. One disadvantage of the method is the difficulty in correctly modeling the boundaries.

The implementation of the method is straightforward and can handle complex free-surface problems and conserves mass. However, the accuracy is limited for multidimensional flows and depend on the number of particles used.

In the case of free-surface flows, specifically air-water flows, an essential requirement for the numerical approaches is the robust solution concerning breaking waves. For most practical applications, the exact modelling of the breaking is not necessary. However, the evaluation of the global effect of forces produced by the breaking waves is mandatory. Another requirement is that the methods are stable even at high Courant numbers to use practical time-steps and reduce computational time.

### 1.3. Numerical Methods for tracking fluid-structure interface

The computation of the fluid-structure interface should be treated as a sharp interface. Thus, some combined Lagrangian-Eulerian methods are the most appropriate.

#### 1.3.1. Immersed boundary methods

The immersed boundary method was firstly used by (Peskin, 1977) to estimate the blood interaction with heart valves.

The domain is fixed, and a polynomial fitting defines the interface. The method generates a diffusive interface, and the information near the interface is smeared over a few cells. Thus, the interface thickness is in order of the mesh size (Fekken, 2004). A Heaviside step function smoothly defines the fluid and solid subdomains. The forces at the interface are considered an integral source term in the momentum equation.

### 1.4. Numerical Methods for modeling fluid-structure interaction (FSI) problems

In general, there are two main approaches to model FSI problems, the monolithic approach or partitioned approach.

The monolithic approach solves the fluid, structure, and interface equations simultaneously in a single and specialized solver. The procedure results in an inherent coupling between the subfields. Thus, the interpolation of the loads and the changes between the computational grids of the subfields are not required.

In contrast, in the partitioned approach, the domain is decomposed in non-overlapping domains for the flow and the structure. Then, two separate field solvers solve the fluid dynamics and the structure dynamic in an iterative process and explicitly use the interfacial conditions to relate information between fluid and structure solutions. Often the Lagrangian formulation is preferred for

---

the solid part since the deformation has to be determined from a known reference configuration, which can be done by tracking the corresponding material points. In contrast, the Eulerian formulation is usually applied for the fluid part since the pressure and velocity at a specific location of the problem domain can be determined (Schäfer, 2006), and generally the mesh for the flow domain is much finer than for the structure domain. The main challenge with this approach is the coupling of the solvers at the fluid-structure interface, which requires techniques to exchange information over the interface and the corresponding interpolation algorithms to interpolate the loads and displacements between the non-matching meshes (de Boer, van Zuijlen, & Bijl, 2007).

The monolithic methods generally are more robust and sometimes more efficient than partitioned schemes (Degroote, Bathe, & Vierendeels, 2009). However, the formulation must be adapted to each problem, so it is less versatile than the partitioned approach. Because of this, nowadays, the partitioned approach is the most applied approach due to its modularity and the possibility of re-using existing software (Kassiotis, Ibrahimbegovic, & Matthies, 2010). Furthermore, more complex computation such as multiphase flows, or turbulence in the fluid part or hyperelastic materials in the structural part can be solved. For this reason, the partitioned approach is used as FSI approach in this work.

In partitioned fluid-structure interaction problems, the solvers act as black-boxes with a given input-output relation at the common boundary. Regularly, the fluid solver receives velocities as an input and returns forces as an output. The structure solver takes forces as an input and returns displacements. The coupling conditions between flow and structural equations are not part of a large system of the fluid or structural equations (Mehl et al., 2016). The classical method to couple fluids and structures solvers is a staggering execution: in each new iteration, the velocity and boundary position calculated from displacements are prescribed in the fluid solver, then it calculates the pressure that is transferred to the structure solver as a surface load on the interface fluid-solid in the structure domain to solve the displacement. The convergence occurs when the difference between the velocities of the fluid and the solid boundary is less than the acceptable error. Serial execution of the coupling often becomes slow, and the parallel implicit coupling can overcome the problem (Mehl et al., 2016).

## **1.5. Fluid-structure interaction involving free surface flows**

### **1.6. Scope and Objectives**

Although several approaches have been developed to predict the fluid-structure interaction in the context of multiphase flows, there are still many challenges to combine the two fields and to simulate more complex real systems. Mainly due to the limitations of the solving algorithms in getting stable when second-order derivatives are involved in the governing equations. Therefore, the principal objective of this work is to develop, investigate, and apply computational methods that allow a reliable simulation of fluid-structure interactions involving free-surface flows with high numerical efficiency.

The problem will be focused on a partitioned FSI approach. On the one hand, the fluid-dynamics will be solved in solver FASTEST where the domain is discretized using the finite volume method (FVM) and block-structured meshes. On the other hand, the solid part will be computed with a finite element method (FEM) in the solver CALCULIX. The two solvers are coupled with an implicit method in the multiphysics environment preCICE. Consequently, the specific research aims of this project are:

### **1.7. Outline**

---

## 2. Mathematical modeling of the physical phenomena

---

**Abstract** The chapter provides an overview of the conservation principles governing the fluid-structure interaction involving a free-surface flow phenomenon. Including a compact mathematical description of multifluid-flows, specifically two-fluid flows, elastic structures, and the treatment for the fluid-structure interface. The principles of conservation of the flow and structure are translated into partial differential equations using the Arbitrary Lagrangian-Eulerian description and the Lagrangian description, respectively.

### 2.1. The problem definition and modeling approaches

A free surface flow interacting with an elastic structure is a multiphysics transient phenomenon. The problem domain  $\Omega$  illustrated in Fig. 2, consists of a two-fluid flow part and a structural part denoted by  $\Omega_f^{1,2}$  and  $\Omega_s$ , respectively. The subscript  $f$  refers to the fluid domain and the subscript  $s$  to the solid part. The fluid-structure interface  $\Gamma_{fs}$  is the boundary where the flexible structure interacts with the fluid and  $\Gamma_f$  is the flow interface between the two fluids. The dynamics of the flow domain are governing by the principle of conservation of mass and momentum formulated using the Arbitrary Lagrangian-Eulerian (ALE) description. In contrast, the structure deformation follows the principles of an elasticity model developed in the framework of the Lagrangian description.

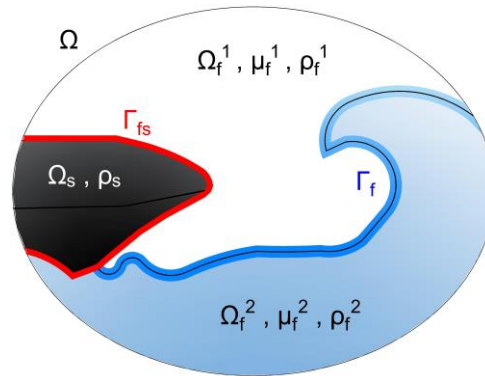


Fig. 2 Problem domain of the fluid-structure interaction involving a free-surface flow phenomenon, the subscripts  $s$  refers to the structure and  $f$  to the fluid. The red line is the fluid-structure interface and the blue line the interface between the two fluids.

In continuum mechanics, the Lagrangian, Eulerian, and ALE approaches describe the changes of material properties during the motion and are used to express the conservation laws mathematically.

In the Lagrangian or material description, the continuum is subdivided into material points, and every material point is followed as it moves along its pathline (Schäfer, 2006). The properties are a function of the position of the material point in time, referred to its initial configuration. Thus, facilitating the treatment of materials with history-dependent behavior, so the Lagrangian approach is mainly used in structural mechanics. However, since the computational mesh moves with the material, when large distortion in the motion occurs, e.g. vortices in fluids, frequent remeshing is necessarily causing a loss of accuracy.

The problems caused by large distortions are overcome in the Eulerian or spatial description, so it is very popular to solve fluid mechanics. The Eulerian approach divides the domain into regions and measures in each specific region the changes in properties of the material particles that are crossing it (F. Moukalled, Mangani, & Darwish, 2016). The material properties have only instantaneous

significance in a fixed region of space and are expressed as functions of position and time without any reference to the initial configuration. The computational mesh is fixed, and the grid nodes are dissociated from the material particles which on the one hand facilitates the handle of complex material movements but on the other hand, includes the convection effects in the formulation increasing the numerical difficulties. Further, the definition of interfaces is less precise than in the Lagrangian approach and has difficulties in working with mobile boundaries.

The Arbitrary Lagrangian-Eulerian description is a generalization of the Lagrangian and the Eulerian frameworks and attempts to overcome their weaknesses. In the ALE description, a third domain that can be mapped from either the material domain or the spatial domain is considered as the reference domain. This third domain represents the temporal variation of a reference space holding a material particle fixed. Thus, the computational mesh can arbitrarily move with a convective velocity that is the relative velocity between the material and the mesh. A comprehensive explanation of the approach is given in (Donea, Huerta, Ponthot, & Rodríguez-Ferran, 2017). The freedom in moving the computation domain in ALE approach allows a greater deformation of the material than the Lagrangian approach with more precision than the Eulerian approach. Therefore, the ALE description applies for formulating large distortion response of materials and fluid-structure interaction problems.

After this general idea about the different approaches for developing the mathematical formulation of the conservation laws, the coming section introduces the mathematical model for two-fluid flow in ALE framework. Then, the development of the elastic model in the Lagrangian description is presented, and the defining the fluid-structure interface boundary conditions closes the chapter

## 2.2. Two-fluid flow domain

The fluid domain  $\Omega_f$  is a multifluid flow formed by two incompressible, viscous, immiscible, and isothermal Newtonian fluids. For modeling purposes, however, the two fluids are assumed as a single continuum effective fluid with varying physical properties that change abruptly across the fluid interface (Tryggvason et al., 2001). Consequently, the same equations that govern a single fluid flow can be applied to a multifluid flow. Although, the stress concentrated at the sharp interface, also called surface tension, must be included in the formulation, and tracking the instantaneous position of two fluids requires the application of an additional equation. Furthermore, due to the fluid-structure interface is a mobile interface that induces distortion of the flow domain, the conservation laws should be formulated in the ALE framework to be able following the structural motion without losing accuracy.

As a result, the two-fluid incompressible flow is described by the one-fluid formulation of the mass, and the momentum conservation equations and the volume fraction transport equation (Hirt & Nichols, 1981) expressed as

$$\nabla \cdot \mathbf{v}_f = 0, \quad (2.1)$$

$$\rho_f \frac{\partial \mathbf{v}_f}{\partial t} + \rho_f (\mathbf{v}_f - \mathbf{v}_g) \cdot \nabla \mathbf{v}_f = \nabla \cdot \boldsymbol{\tau}_f + \mathbf{B}, \quad (2.2)$$

$$\frac{\partial \alpha}{\partial t} + (\mathbf{v}_f - \mathbf{v}_g) \cdot \nabla \alpha = 0, \quad (2.3)$$

where  $\mathbf{v}$  is the fluid velocity,  $\rho$  the density,  $\mathbf{v}_g$  the arbitrary grid velocity introduced by the ALE approach.  $\boldsymbol{\tau}$  is the stress tensor,  $\mathbf{B}$  the body forces, and  $\alpha$  the volume fraction of one of the fluids.

For Newtonian incompressible fluids, the stress tensor is assumed to be a linear function of the rate of strain tensor (Ferziger, Perić, & Street, 2020) and is defined with the Stokes law as

$$\boldsymbol{\tau}_f = -p\mathbf{I} + \mu_f \left\{ \nabla \mathbf{v}_f + (\nabla \mathbf{v}_f)^T \right\}, \quad (2.4)$$

where  $\mu$  is the dynamic viscosity,  $p$  is the pressure and  $\mathbf{I}$  is the identity.

Moreover, the body force term for multiphase flows is the sum of the gravitational forces and the surface tension effects given by

$$\mathbf{B} = \rho_f \mathbf{g} + \gamma_f \kappa_f \mathbf{n}^{\Gamma_f} |\nabla \alpha|, \quad (2.5)$$

where  $\mathbf{g}$  is the gravity,  $\gamma$  the constant surface tension coefficient, the Gaussian curvature  $\kappa$  of the fluid interface, and  $\mathbf{n}^{\Gamma_f}$  the outward normal to the interface between the two fluids. Here the surface tension effects, the second term, is expressed as a volume force acting in a normal direction towards the fluid interface. The formulation of this term can be found in detailed in (Wacławczyk, 2007).

The interface shape determines the influence of the gravitational forces or the surface tension in the flow dynamic. When the radius of the interface curvature tends to infinity, e.g. water waves, the curvature tends to zero, and the surface tension vanishes. Whereas for small curvatures radius, e.g. a small water droplet, the surface tension is dominant, and the gravity force is neglected.

Substituting the expressions for the stress tensor, and body forces into the momentum equation (Eq. 2.2) and assuming constant viscosity results in

$$\rho_f \frac{\partial \mathbf{v}_f}{\partial t} + \rho_f (\mathbf{v}_f - \mathbf{v}_g) \cdot \nabla \mathbf{v}_f = -\nabla p + \mu_f \nabla^2 \mathbf{v}_f + \rho_f \mathbf{g} + \gamma_f \kappa_f \mathbf{n}^{\Gamma_f} |\nabla \alpha|. \quad (2.6)$$

The above expression represents the equation of motion in the convective or non-conservative form usually used for incompressible flows with a density that changes abruptly because the conservative form can lead to numerical difficulties (Tryggvason et al., 2001).

Finally, notice that the momentum equation (Eq. 2.6) uses averages values of the material properties that are recovered from the volume fraction and individual material properties of each constituent fluid by

$$\rho_f = \alpha \rho_f^1 + (1 - \alpha) \rho_f^2, \quad \mu_f = \alpha \mu_f^1 + (1 - \alpha) \mu_f^2. \quad (2.7)$$

That are an algebraic statement of local mass conservation.

### 2.3. Elastic structural domain

When the elastic deformation of the structure is a partial aspect of the fluid-structure interaction coupling, the structural domain needs to be mathematically modelled with an elasticity model. To describe how the solid object reversibly deforms and becomes internally stressed due to flow-induced loads.

An elasticity model is based on the kinematics, Newton's second law, and a constitutive law and is used to determine all the stresses, strains, and displacements that the elastic body experiences after having moved from its reference state. The *kinematics* describes the motion of the object and is the relationship between displacement and strain. The motion can be translation, rotation, or deformation of the solid. Instead, the linear momentum equation also called *Newton's second law of motion* states the balance of the deformation and related stress. Whereas, the *constitutive law* relates strain and stresses,

and models the specific behavior of the material, including the material properties in the definition of the structural domain. A good explication of the elastic model can be found in (Dhondt, 2004; Fung, 1965).

The measures of the deformation are the displacement and the Lagrangian strain tensor. The displacement  $\mathbf{u}_s = \mathbf{x} - \mathbf{X}$  is the vector connecting the undeformed reference configuration  $\mathbf{X}$  of a material particle to its deformed current configuration  $\mathbf{x}$  at time  $t$ . The displacement is the measure of the change from  $\mathbf{X}$  to  $\mathbf{x}$  regardless of the real size of  $\mathbf{x}$ . On the other hand, the Lagrangian strain tensor or sometimes called Green-Lagrange strain tensor  $\boldsymbol{\varepsilon} = \frac{1}{2}(\mathbf{F}^T \cdot \mathbf{F} - \mathbf{I})$  establishes a relationship between the displacements and the distortions and can be interpreted as measures for the change of length in a body. Where  $\mathbf{F} = d\mathbf{x}/d\mathbf{X}$  is the deformation gradient which represents the Jacobian matrix of the motion from the reference into the final state.

The motion of the body is described by the instantaneous velocity field defined as  $\mathbf{v}_s = d\mathbf{u}_s/dt$  and obeys the Newton's second law that in Lagrangian coordinates is expressed as

$$\rho_s \frac{\partial^2 \mathbf{u}_s}{\partial t^2} = \nabla (J \boldsymbol{\sigma}_s \mathbf{F}^{-T}) + \rho_s \mathbf{g} \quad (2.8)$$

where  $\rho_s$  is the solid density,  $J = \det(\mathbf{F})$  is the Jacobian, and  $\boldsymbol{\sigma}_s$  is the Cauchy stress tensor field which is considered as the real stress because it is defined in the spatial state of reference.

To close the formulation of the structural problem, the Cauchy stress tensor is defined according the used material. In this investigation, only the isotropic linear elastic materials and isotropic hyperelastic materials are of interest. Therefore, a short introduction about them is given below.

The isotropic linear elastic material model also called St Venant-Kirchhoff material is characterized by an elastic potential in which only the quadratic terms are retained in the deformation  $\boldsymbol{\varepsilon} = \frac{1}{2}(\nabla \mathbf{u}_s + \nabla \mathbf{u}_s^T)$ . The constitutive law is:

$$\boldsymbol{\sigma}_s = 2\mu_s \boldsymbol{\varepsilon} + \lambda_s \text{tr}(\boldsymbol{\varepsilon}) \mathbf{I}, \quad (2.9)$$

where  $\lambda$  and  $\mu$  are the Lamé constants which depend on the properties of corresponding material, the Young's module, or module of elasticity  $E$  and Poisson's coefficient  $\nu$ . The relation between these quantities are:

$$\lambda = \frac{\nu E}{(1+\nu)(1-2\nu)}, \quad \mu = \frac{E}{2(1+\nu)}. \quad (2.10)$$

The linear elastic model is applicable for materials with  $\nu < 0.5$ . Conventional steels, some plastics, glass, and concrete are usually in this category. Mandatory prerequisites are that the stresses are not too big, and the deformation occurs within the elastic range of the material (Schäfer, 2006)

On the other hand, for the isotropic hyperelastic materials, e.g. rubber, the resulting stress is not necessarily linear in  $\boldsymbol{\varepsilon}$ . For this material, the potential function is a function of the strain invariants only. Due to the complexity of this topic and the large family of models that covers these materials, their description is omitted here, instead the reader is encouraged to review more specialized literature such as (Dhondt, 2004, 2012) in which the implementation in Calculix of the neo-Hooke, Mooney-Rivlin, Ogden and many other hyperelastic models is given in detail.

---

Regarding the solution of these governing equations the reader is

#### 2.4. Interaction conditions

Finally, the problem formulation is closed by prescribed suitable boundary and interface conditions. On solid and fluid boundaries  $\Gamma_s$  and  $\Gamma_f$  standard conditions as for individual solid and fluid problems can be prescribed. Whereas in the fluid-structure interface, the dynamic and kinematic conservation has to be satisfied. That means that the forces are assumed in balance, and no-slip boundary conditions are set in the flow domain.

$$\mathbf{v}_f = \mathbf{v}_s \quad \text{and} \quad \boldsymbol{\sigma}_s \mathbf{n}^{\Gamma_{fs}} = \mathbf{T} \mathbf{n}^{\Gamma_{fs}}, \quad (2.11)$$

where  $\dot{\mathbf{u}}_s$  is the velocity of the solid at the interface, and  $\mathbf{n}^{fsi}$  is the normal unit vector to the interface  $\Gamma_{fsi}$ .

### 3. Discretization of the fluid domain

**Abstract** This chapter details the discretization process of the fluid domain. In the present research work, the finite volume method is used for the spatial discretization of the equations and the finite difference method for the time discretization. The finite volume method is a second-order method that transforms the partial differential equations into a system of linear algebraic equations. First, the flow domain is divided into control volumes, and then the partial equations are integrated and transformed into balance equations over every control volume. This requires changing the surface and volume integrals into discrete algebraic relations over control volumes and their surfaces applying an integration quadrature. As a result, a set of semi-discrete equations are created. The second step is to select interpolation profiles to approximate the derivation of variables within the cell and to match the surface in algebraic equations.

The following sections will be dedicated to the discretization the most relevant terms of the momentum equation that influence the calculation of multiphase flows. The methods and implementation presented in this section are built on the version of the flow solver FASTEST-3D (Durst & Schäfer, 1996) from the institute of numerical methods for mechanical engineering of the TU-Darmstadt.

The final form of the general conservation equation for the transport of a property  $\phi$  is expressed as

$$\underbrace{\frac{\partial(\rho\phi)}{\partial t}}_{\text{unsteady term}} + \underbrace{\nabla \cdot (\rho \mathbf{v} \phi)}_{\text{convective term}} = \underbrace{\nabla \cdot (\Gamma^\phi \nabla \phi)}_{\text{diffusion term}} + \underbrace{Q^\phi}_{\text{source term}} \quad (2.12)$$

#### 3.1.1. Spatial discretization of the fluid domain

All discretization methods first require the discretization of the spatial problem domain. This is done by the definition of a suitable grid structure covering the physical problem domain. In FASTEST-3D, the grid is defined dividing the physical space into several arbitrary hexahedral control volumes which form a block-structured grid. A block-structured grid is characterized by a regular arrangement of the grid cells, thereby the neighboring relation between the grid points follow a particular fixed pattern which simplifies the discretization process (Schäfer, 2006).

The finite difference method and the finite volume method implemented in the FASTEST solver is built on a Cartesian coordinate system. Therefore, the generally irregular and curvilinear physical domain (global coordinates) has to be mapped to a regular Cartesian one (local coordinates) as is depicted in Fig. #.

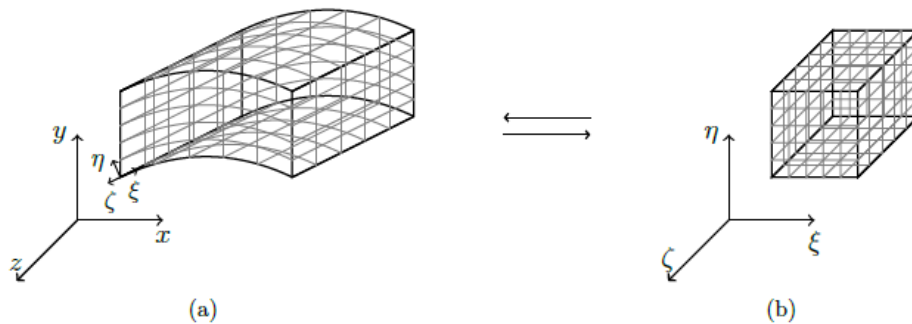


Abbildung 3.1: Koordinatentransformation vom physikalischen Gebiet (a) zum Rechengebiet (b).



The global coordinates system is denoted by  $\mathbf{x}_i = (x, y, z)$  and the local coordinate system by  $\xi_j = (\xi, \eta, \zeta)$ . The mapping between the two coordinate systems  $\mathbf{x}_i = \mathbf{x}_i(\xi_j)$ ,  $j = 1, 2, 3$  is performed with the transformation matrix  $b_{ij}$

$$\mathbf{b}_{ij} = \left( \frac{\partial \mathbf{x}_i}{\partial \xi_j} \right) = \begin{bmatrix} \frac{\partial x}{\partial \xi} & \frac{\partial x}{\partial \eta} & \frac{\partial x}{\partial \zeta} \\ \frac{\partial y}{\partial \xi} & \frac{\partial y}{\partial \eta} & \frac{\partial y}{\partial \zeta} \\ \frac{\partial z}{\partial \xi} & \frac{\partial z}{\partial \eta} & \frac{\partial z}{\partial \zeta} \end{bmatrix}. \quad (3.1)$$

The components of the transformation matrix are approximated with the second-order central differences method that depends on the topology of the control volumes. In FASTEST-3D, a control volume is defined by eight vertices point (1-8) and a center point P as is shown in Fig. #. The centers of the surrounding control volumes are identified by W, E, S, N, B and T, which refer to west, east, south, north, bottom, and top, respectively. The designation corresponds to the orientation of the adjacent centers for point P. The center of the faces of the control volume is identified by corresponding lower case letters (w,e,s,n,b,t).

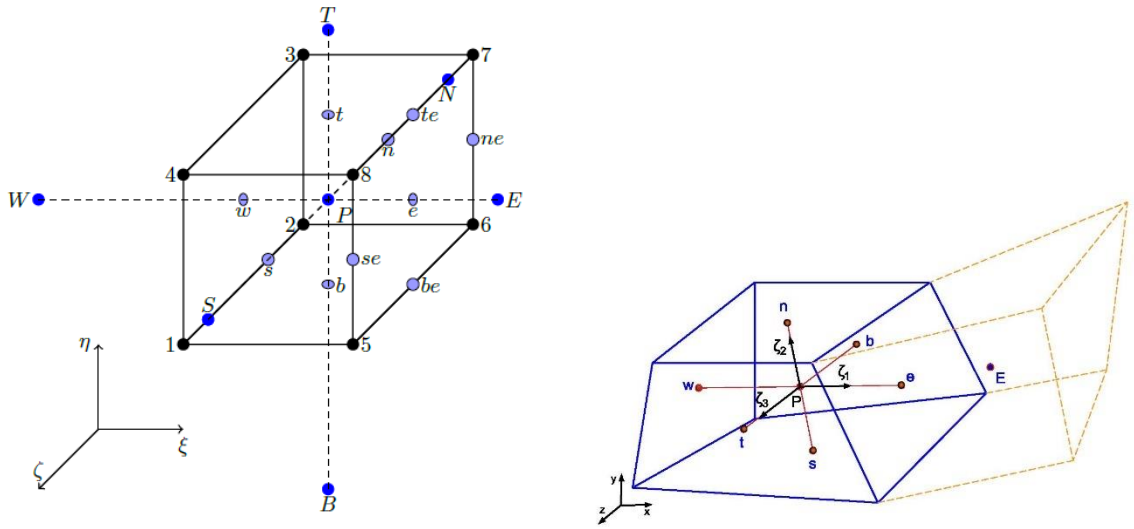


Fig. 3 The topology of a control volume in the FASTEST-3D. The local coordinate system defined in the center of the control volume P.

For example, if the local axis origin is in the center of the control volume P, the element  $b_{11}$  is defined as:

$$(b_{11})_P = \left( \frac{\partial x}{\partial \xi} \right) \approx \frac{x_e - x_w}{\Delta \xi} \quad (3.2)$$

where  $\Delta \xi = 1$  is here generally assumed. The coordinates  $x_e$ , and  $x_w$  are not directly known and are interpolated from the surrounding grid coordinates

$$(b_{11})_P \approx x_e - x_w = \frac{x_5 + x_6 + x_7 + x_8}{4} - \frac{x_1 + x_2 + x_3 + x_4}{4}. \quad (3.3)$$

For more information about the coordinate transformation, the reader can review (Münsch, 2015).

Since the global coordinates system is used in the discretization, the derivatives concerning global coordinates need to transform into the local coordinates applying the chain ruler:

$$\frac{\partial \phi}{\partial \mathbf{x}_i} = \frac{\partial \phi}{\partial \xi_j} \frac{\partial \xi_j}{\partial \mathbf{x}_i} = \frac{\partial \phi}{\partial \xi_j} \mathbf{b}_{ij}^{-1} = \frac{\partial \phi}{\partial \xi_j} \frac{\beta_{ij}}{J} \quad (3.4)$$

where  $J = \det(\mathbf{b}_{ij})$  is the Jacobian and  $\beta_{ij} = \text{adj}(\mathbf{b}_{ij})$  is the adjoint of the transformation matrix,

The generic convective/diffuse transport equation in computational domain results in

$$\frac{\partial(\rho\phi)}{\partial t} + \frac{1}{J} \frac{\partial}{\partial \xi_j} (\rho\phi \mathbf{V}_j) = \frac{1}{J} \frac{\partial}{\partial \xi_j} \left( \frac{\Gamma^\phi}{J} \frac{\partial \phi}{\partial \xi_k} B_{kj} \right) + Q^\phi \quad (3.5)$$

where

$$\mathbf{V}_j = v_m \beta_{mj} = v_1 \beta_{1j} + v_2 \beta_{2j} + v_3 \beta_{3j} \quad (3.6)$$

represent the contravariant velocity, which is proportional to the velocity component normal to the coordinate surface  $\xi_j$ . The coefficients  $B_{kj}$  are mixed coefficients with unequal indexes defined as:

$$B_{kj} = \beta_{mj} \beta_{mk} = \beta_{1j} \beta_{1k} + \beta_{2j} \beta_{2k} + \beta_{3j} \beta_{3k}, \quad (3.7)$$

which become zero when the grid is orthogonal, either it is rectilinear or curvilinear.

Equation (2.3) retains the form of equation (1.11), but each derivative consists of the sum of three terms whose coefficients are the derivatives of the coordinates. For the convective term, it is not a difficulty, but for the diffusive term, the coefficient  $B_{kj}$   $k \neq j$  multiplying the mixed derivatives can cause numerical problems in non-orthogonal grids. Because the coefficients of the mixed derivatives can be higher than the diagonal coefficient  $B_{jj}$  when the angle between grid lines is small, and the aspect ratio is large (Ferziger et al., 2020). The mixed derivatives are explicitly addressed to prevent this problem,

### 3.1.2. Discretization of the equations

The fluid domain is discretized in space with the second-order Finite Volume Method (FVM) and in time with the finite difference approach. A detailed explanation of them can be found in (Ferziger et al., 2020; F. H. Moukalled, Mangani, & Darwish, 2016) and more specific aspects related to multiphase flow systems in the doctoral work of Sauer (Sauer, 2000) or Waławczyk (Waławczyk, 2007).

The first step for the spatial discretization using FVM is to integrate the governing equations over each control volume and to apply the Gauss theorem, and the volume integrals are transformed to surface integrals over the boundary  $\mathbf{S}$  that closes the volume  $V$  of the cell. Following these steps, the equation (#) results in

$$\int_S \mathbf{v}_f \cdot \mathbf{n} dS = 0 \quad (3.8)$$

$$\underbrace{\rho \frac{d}{dt} \int_V \mathbf{v} dV}_{\text{transient term}} + \underbrace{\int_S \rho (\mathbf{v} - \mathbf{v}_g) \mathbf{v} \cdot \mathbf{n} dS}_{\text{convective term}} = \underbrace{- \int_S p \cdot \mathbf{n} dS}_{\text{pressure term}} + \underbrace{\int_S \mu \left( \frac{\partial \mathbf{v}_i}{\partial \mathbf{x}_j} + \frac{\partial \mathbf{v}_j}{\partial \mathbf{x}_i} \right) \cdot \mathbf{n} dS}_{\text{diffusion term}} + \underbrace{\int_V (\rho \mathbf{g} + \sigma \kappa \mathbf{n} |\nabla \alpha|) dV}_{\text{source term}} \quad (3.9)$$

$$\frac{\partial}{\partial t} \int_V \alpha dV + \int_S (\mathbf{v} - \mathbf{v}_g) \alpha \cdot \mathbf{n} dS = 0 \quad (3.10)$$

where  $\mathbf{n}$  is the normal vector to the volume surface and directed outwards. The grid velocity is determined with the discrete form of the space conservation law (SCL) (Demirdžić & Perić, 1988) given by

$$\frac{d}{dt} \int_V dV - \int_S \mathbf{u}_g \cdot \mathbf{n} dS = 0. \quad (3.11)$$

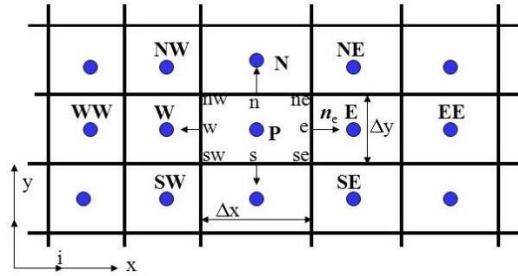


Fig. #. 2D fluids domain discretized by Finite volume method

### 3.1.3. Discretization of the momentum equation

Replacing the surface integral over an arbitrary cell P by a summation of the flux terms over the faces of cell P, the surface integral of the diffusion become

$$\int_S \mu \left( \frac{\partial \mathbf{v}_i}{\partial \mathbf{x}_j} + \frac{\partial \mathbf{v}_j}{\partial \mathbf{x}_i} \right) \cdot \mathbf{n} dS = \sum_{f=1}^{nb} \left( \mu \frac{\partial \mathbf{v}_i}{\partial \mathbf{x}_j} \mathbf{n}_j S \right)_f + \sum_{f=1}^{nb} \left( \mu \frac{\partial \mathbf{v}_j}{\partial \mathbf{x}_i} \mathbf{n}_i S \right)_f = \sum_{f=1}^{nb} F_{i,f}^{D_1} + \sum_{f=1}^{nb} F_{i,f}^{D_2} = \sum_{f=1}^{nb} F_{i,f}^D$$

Of this expression, the first diffusive flux  $F_{i,f}^{D_1}$  is included in the convection term, and the second term  $F_{i,f}^{D_2}$  is included in the source term.

The total diffusive flux is calculated with a deferred correction method using a higher  $H$  and lower  $L$  order of discretization and with a diffusive blending factor  $\beta^D$ ,

$$F_{i,f}^D = F_{i,f}^{D_1,L} + \beta^D (F_{i,f}^{D,H} - F_{i,f}^{D_1,L})$$

where the higher-order discretization of the whole viscous part is

$$F_{i,f}^{D,H} = \left[ \mu n_j S \left( \frac{\partial u_i}{\partial x_j} + \frac{\partial u_j}{\partial x_i} \right) \right]_f$$

here the velocity gradients are firstly defined at the center of the control volume and secondly that interpolated to obtain the value on the face of the control volume.

Whereas the lower order discretization of the first term of diffusive flux is:

$$F_{i,f}^{D1,L} = \left[ \mu \left( \frac{\partial u_i}{\partial x_j} n_j S \right) \right]_f \approx \frac{u_{i,F} - u_{i,P}}{\delta n_{P,F}} u_f S_f$$

where  $\delta n_{P,F} = \overline{x_F} - \overline{x_P}$ ,  $u_i$  is the velocities in the center of the control volume and  $S_f$  is the area of the face.

However, using this discretization in non-orthogonal grids, an oscillatory solution may appear. Since the face center is not part of the line between the nodal points near the face. The convective/diffusive equation should be reformulated in a local reference frame to avoid this problem (Wacławczyk, 2007)

The local reference frame is defined by three vectors  $\vec{\zeta}_1, \vec{\zeta}_2, \vec{\zeta}_3$  associated with the face f of the control volume V, as illustrated in Fig. 3.3.

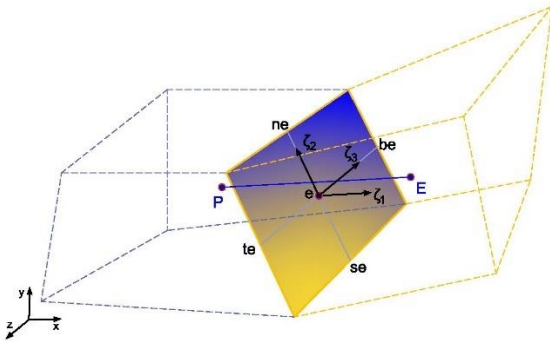


Figure 3.3 Control volume P and its east neighbor E with local coordinate system defined by the vectors  $\vec{\zeta}_1, \vec{\zeta}_2, \vec{\zeta}_3$  on the face f=e

Then, the variable  $u_i$  is changed from the global to local reference frame using the transformation matrix between the two coordination systems  $A_{ij} = \partial x_i / \partial \zeta_j$ , following the next expression,

$$\frac{\partial u_i}{\partial x_j} = \frac{\partial \zeta_i}{\partial x_j} \frac{\partial u_i}{\partial \zeta_i} = A_{ij}^{-1} \frac{\partial u_i}{\partial \zeta_i}$$

where  $A_{ij}$  has non-zero Jacobian determinant ( $J$ ) to change the frame of reference.

$$A_{ij}^{-1} \frac{\partial u_i}{\partial \zeta_j} = \frac{1}{J} \left[ adj(A_{ij}) \right]^T = \frac{1}{J} \beta_{ji}$$

where  $\beta_{ji}$  is estimated using a discretized matrix  $b_{ij}$  of dimension (3x3) that contains the vector components of the three vectors associated with the face geometry, for more details see Ref. (Wacławczyk, 2007).

$$\beta_{ji} \approx \frac{1}{\Delta \zeta_k \Delta \zeta_l} b_{ji}$$

$$b_{ji}^S = \begin{pmatrix} \Delta_2 x_2 \Delta_3 x_3 - \Delta_2 x_3 \Delta_3 x_2 & \Delta_2 x_3 \Delta_3 x_1 - \Delta_2 x_1 \Delta_3 x_3 & \Delta_2 x_1 \Delta_3 x_2 - \Delta_2 x_2 \Delta_3 x_1 \\ \Delta_3 x_2 \Delta_1 x_3 - \Delta_1 x_2 \Delta_3 x_3 & \Delta_1 x_1 \Delta_3 x_3 - \Delta_3 x_1 \Delta_1 x_3 & \Delta_1 x_2 \Delta_3 x_1 - \Delta_3 x_2 \Delta_1 x_1 \\ \Delta_1 x_2 \Delta_2 x_3 - \Delta_1 x_3 \Delta_2 x_2 & \Delta_1 x_3 \Delta_2 x_1 - \Delta_1 x_1 \Delta_2 x_3 & \Delta_1 x_1 \Delta_2 x_2 - \Delta_1 x_2 \Delta_2 x_1 \end{pmatrix}$$

The superscript S denotes the vector components associated with the face that is calculated with the following formulas,

$$\zeta_{1,i} = \Delta_1 x_i = x_{E,i} - x_{P,i} \quad i=1,2,3$$

$$\zeta_{2,i} = \Delta_2 x_i = x_{ne,i} - x_{se,i} \quad i=1,2,3$$

$$\zeta_{3,i} = \Delta_3 x_i = x_{te,i} - x_{be,i} \quad i=1,2,3$$

Under those considerations, the momentum equation in the local reference system is rewritten considering a new source term  $S_{u_i}$  which groups all the terms of the right side of Eq. (3.18).

$$\int_V \frac{\partial(\rho u_i)}{\partial t} dV + \int_S \left( u_i \rho u_j - \frac{\mu}{J} \frac{\partial u_i}{\partial \zeta_j} \beta_{ji} \right) n_j dS = \int_V S_{u_i} dV$$

Regarding this reformulated equation, the term directly affected is the first part of the diffusion term. Therefore, It is discretized again,

$$F_{i,f}^{D_1,L} = \int_S \frac{\mu}{J} \frac{\partial u_i}{\partial \zeta_i} \beta_{ji}^S n_j dS \approx \sum_{f=1}^{nb} \left( \frac{\mu}{J \delta V} b_{ji}^S b_{jm}^S \Delta_i u_i \right)_f$$

where  $\partial u_i / \partial \zeta_i$  was approximated as  $\Delta_i u_i / \Delta \zeta_i$ ,  $\delta V = \Delta \zeta_1 \Delta \zeta_2 \Delta \zeta_3$  is an auxiliary control volume and  $m$  is equal to 1, 2 or 3 depending on the face of the control volume employed for flux calculation, i.e., east  $e$ , west  $w$ , or north  $n$ , respectively.

### 3.1.4. Green Gauss gradient with the midpoint correction for non-orthogonal grids

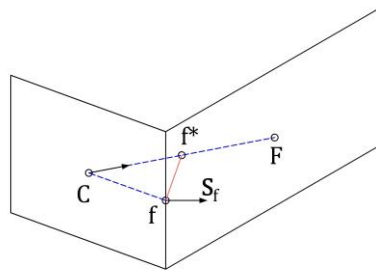


Fig. 4 The connection between two non-orthogonal control volumes using the midpoint approach in a two-dimensional configuration.

The calculation of the gradient field over the domain is an iterative process that proceeds as follows:

During the first iteration, calculate the gradient field as follows:

1. Calculate the face value  $\phi_{f*} = \frac{\phi_C + \phi_F}{2}$

2. Calculate the Green Gauss gradient  $\nabla\phi_C = \frac{1}{V_C} \sum_{f \sim nb(C)} \phi_f \mathbf{S}_f$

From the second iteration onward, correct the gradient field according to the following procedure:

3. Update  $\phi_f = \phi_{f*} + \frac{[\nabla\phi_C + \nabla\phi_F]}{2} \cdot \left[ \mathbf{x}_f - \frac{\mathbf{x}_C + \mathbf{x}_F}{2} \right]$
4. Update  $\nabla\phi_C = \frac{1}{V_C} \sum_{f \sim nb(C)} \phi_f \mathbf{S}_f$
5. Go back to step 3 and repeat

### 3.1.5. Face values of density and viscosity

The issue of accurate viscous stress modelling at fluid interfaces – e.g., correct capturing of the viscosity term within at the free-surface is a quite important one, though not being addressed often in the literature dealing with the VOF approach: it is common practice to use the arithmetic mean as for the mixture viscosity is being done for the mixture density. However, being confronted with free-surface flows possessing gross and abrupt changes of the viscosity across the interface the correct evaluation of  $\mu$  at the interface (i.e., the interfacial viscosity) is crucial for reproducing the correct free-surface dynamics in numerical simulations. Only using arithmetic mean causes an artificial (increased) acceleration of fluid elements in the lighter phase which yields too high velocities due to an unphysical viscous term

The harmonic mean is more accurate when the interface tends to be aligned with the Flow direction; nonetheless, it is less robust than arithmetic means inflows with significant density differences.

The cell face viscosity and density are determined using an interpolation factor  $\eta_f$  which accounts for the two-fluid flow interface/cell face orientation, and evaluating the phase value  $\phi_f$  in the limits of a harmonic mean  $\phi^h$  and arithmetic mean  $\phi^a$ , as follow:

$$\phi_f = \eta_f \phi^a + (1 - \eta_f) \phi^h$$

$$\text{Where } \eta_f = \left( \left( \frac{\nabla\alpha}{\|\nabla\alpha\|} \right)_f \cdot \frac{\mathbf{S}_f}{\|\mathbf{S}_f\|} \right) \text{ and } \phi^a = \gamma_F \phi_F + (1 - \gamma_F) \phi_C, \quad \phi^h = \frac{\phi_F \phi_C}{\gamma_F \phi_F + (1 - \gamma_F) \phi_C}$$

here  $\gamma_F = \frac{\|\mathbf{x}_f - \mathbf{x}_C\|}{\|\mathbf{x}_F - \mathbf{x}_C\|}$  is the geometric weighting factor, and the interpolated gradient to the face of the volume fraction is evaluated according to the procedure presented in (F. Moukalled et al., 2016)

$$\nabla\alpha_f = \overline{\nabla\alpha_f} + \left[ \frac{\alpha_F - \alpha_C}{\|\mathbf{x}_C - \mathbf{x}_F\|} - \overline{\nabla\alpha_f} \cdot \mathbf{e}_{CF} \right] \mathbf{e}_{CF}$$

$$\overline{\nabla\alpha_f} = g_C \nabla\alpha_C + (1 - g_C) \nabla\alpha_F, \quad \mathbf{e}_{CF} = \frac{(\mathbf{x}_C - \mathbf{x}_F)}{\|\mathbf{x}_C - \mathbf{x}_F\|}$$

where the nodal gradients are calculated with the Green Gauss gradient with the midpoint correction approach and  $g_C$  is a corrected geometrical weighting factor that can be computed applying the minimum distance approach

$$g_C = \frac{\|\mathbf{x}_F - \mathbf{x}_{f^*}\|}{\|\mathbf{x}_F - \mathbf{x}_C\|}, \quad \text{and} \quad \mathbf{x}_{f^*} = \mathbf{x}_C - \frac{(\mathbf{x}_C - \mathbf{x}_f) \cdot (\mathbf{x}_C - \mathbf{x}_F)}{(\mathbf{x}_C - \mathbf{x}_f) \cdot (\mathbf{x}_C - \mathbf{x}_F)} (\mathbf{x}_C - \mathbf{x}_F)$$

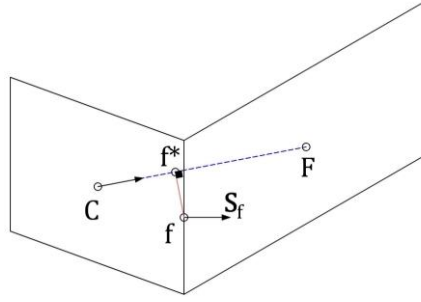


Fig. 5 Connection between two non-orthogonal control volumes using the minimum distance approach in a two-dimensional configuration.

### 3.1.6. Treatment of the Body Force Term

The Rhie-Chow interpolation scheme works well if the pressure field is sufficiently smooth, but if abrupt variations occur, nonphysical spikes in the velocity field can appear near the abrupt variations of the pressure field. The abrupt pressure variation is closely related to the abrupt changes of body forces. This relation becomes clear if we consider the momentum equation for a quiescent fluid ( $\mathbf{v} = 0$ ) that results in

$$0 = -\nabla p + \underbrace{(\rho \mathbf{g} + \sigma \kappa \mathbf{n} |\nabla \alpha|)}_{\mathbf{B}}. \quad (3.12)$$

Then, to avoid unphysical spikes, the pressure gradient should be in equilibrium with the body forces.

In multiphase flows (e.g. gas-liquid) the sudden variation in density results in such as variation in body forces. Another example is bubbles or droplets whose strong surface tension causes abrupt changes of the body forces field in the vicinity of the flow interface.

In order to preserve the equilibrium between body forces and pressure gradient even abrupt changes of the body forces are present and thus to avoid the apparition of the so-called spurious currents, I use the approach introduced by Mencinger (Mencinger, 2012) for collocated grids. The remedy consists in evaluating the body forces in a similar stencil as the pressure which implicates a redistribution of the body force term. This redistribution can best be derived by considering the one-dimensional case illustrated in Fig. 5. The double bar indicates two average steps.

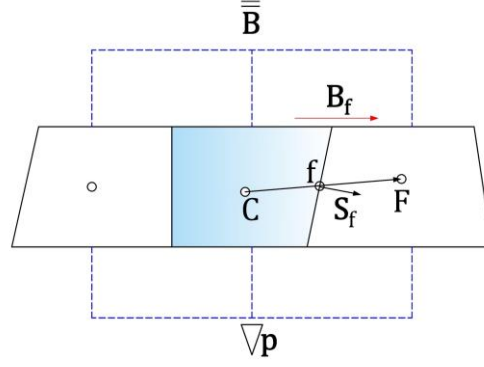


Fig. 6 One dimensional stationary flow

The method begins by assuming that the solution of the momentum equation for a stationary fluid is satisfied on all control volumes faces, thus

$$(\nabla p)_f = \mathbf{B}_f \quad (3.13)$$

when using the Rhie-Chow correction. Then, the dot product of Eq. (2.13) with the vector from point C to F,  $\mathbf{x}_{CF}$ , is applied which results in

$$P_F - P_C = \mathbf{x}_{CF} \cdot \mathbf{B}_f \quad (3.14)$$

where the body force on the face is linearly interpolated from the nodal neighbour values

$$\mathbf{B}_f = \gamma_F \mathbf{B}_F + (1 - \gamma_F) \mathbf{B}_C. \quad (3.15)$$

The second part is applying the condition of a stationary fluid for the central point

$$(\nabla p)_C = \mathbf{B}_C \quad (3.16)$$

where the pressure gradient is computed with the Green Gauss gradient, and the pressure on faces again with linear interpolation

$$(\nabla p)_C = \frac{1}{V_C} \sum_{f \sim nb(C)} p_f \mathbf{S}_f = \frac{1}{V_C} \sum_{f \sim nb(C)} (\gamma_F P_F + (1 - \gamma_F) P_C) \mathbf{S}_f. \quad (3.17)$$

Inserting (2.16) and (2.13) in (2.15) results in

$$\mathbf{B}_C = \frac{1}{V_C} \sum_{f \sim nb(C)} (P_F + \mathbf{x}_{CF} \cdot \mathbf{B}_f) \mathbf{S}_f = \frac{P_F}{V_C} \sum_{f \sim nb(C)} \mathbf{S}_f + \frac{1}{V_C} \sum_{f \sim nb(C)} (\mathbf{x}_{CF} \cdot \mathbf{B}_f) \mathbf{S}_f \quad (3.18)$$

where the first term is equal to zero because  $\sum_{f \sim nb(C)} \mathbf{S}_f = 0$  for any closed surface. Finally,

$$\overline{\mathbf{B}}_C = \mathbf{B}_C = \frac{1}{V_C} \sum_{f \sim nb(C)} (\mathbf{x}_{CF} \cdot \mathbf{B}_f) \mathbf{S}_f \quad (3.19)$$



The above expression represents the re-distributed body forces that have to be used in the momentum equation instead of the direct volumetric body forces to avoid unphysical spikes in the velocity field.

Considering that for FSI cases, the grid is in constant deformation, we applied the expression (2.19). However, the body forces on the faces are interpolated values using the Taylor series expansion approach (TSE) (Lehnhäuser & Schäfer, 2002) instead to the linear interpolation because TSE preserves second-order accuracy even in distorted grids. The TSE interpolation approach defines the face value using the nodal values of the volumes near the face. For example, the force at the east face,  $e$ , of a control volume  $P$  with neighbors  $E$ ,  $N$ ,  $S$ ,  $T$ ,  $B$  located according to Fig. 4 is determined as:

$$\mathbf{B}_e = \gamma_E \mathbf{B}_E + (1 - \gamma_E) \mathbf{B}_P + \gamma_{NS} (\mathbf{B}_N - \mathbf{B}_S) + \gamma_{TB} (\mathbf{B}_B - \mathbf{B}_T)$$

where the  $\gamma$  factors are geometric. More details on how to define these factors are found in (Lehnhäuser & Schäfer, 2002)

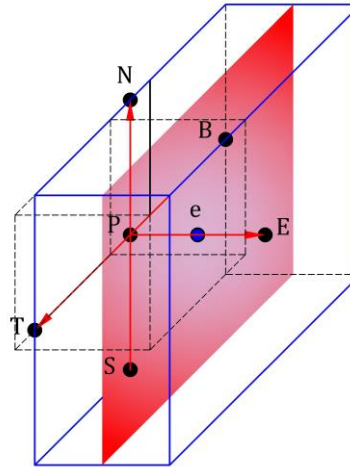


Fig. 7 Volume around the  $e$  face of the control volume  $P$  and location of the neighbour's nodal points to the control volume  $P$

### 3.1.7. Convective term

Although the convection term looks simply

### 3.1.8. Set of linear equations

### 3.1.9. Equilibrium condition and discretization of volume forces

### 3.1.10. Boundary conditions

### 3.1.11. Pressure and velocity coupling

The cell center variable arrangement is used.

---

## **3.2. Discretization of the volume-fraction transport equation**

### **3.2.1. Temporal discretization**

(Gillebaart, Blom, van Zuijlen, & Bijl, 2016) the use of higher-order time integration schemes such as BDF2 in the two solvers increases the efficiency because a larger time step can be used for the same accuracy and without losing stability. Or the use of QS-LNS acceleration methods can be reduced significantly the number of iterations sees for more information

### **3.2.2. Spatial discretization**

### **3.2.3. Normalized variable diagram and high-resolution schemes**

### **3.2.4. Normalized variables on non-uniform and unstructured mesh**

### **3.2.5. Compressive high-resolution schemes**

### **3.2.6. Discretization of surface tension term**

### **3.2.7. Comparison of high-resolution compressive schemes**

---

## 4. Results

---

### 4.1. Code verification of the pressure-velocity coupling algorithm

The code verification is a process by which one demonstrates that a partial differential equation software correctly solves its governing equations (Knupp & Salari, 2002). Here the new proposed pressure-velocity coupling algorithm is verified with the method of manufacturing solutions (MMS). The MMS verifies that the order-of-accuracy of the numerical algorithm employed by the code matches its theoretical order-of-accuracy (Roache, 2002). Salari and Knupp (Knupp & Salari, 2002) provide a comprehensive guide to creating manufactured solutions, as well as the procedure for inserting them into the code and subsequent analysis of the results.

For verification proposes, the fluid solver is set to solve a single incompressible 3D fluid in a fixed domain and without gravity effects, so the governing equations presented in chapter two (Eq.#) become

$$\nabla \cdot \mathbf{v}_f = 0, \quad (3.20)$$

$$\rho \frac{\partial \mathbf{v}_f}{\partial t} + \rho \mathbf{v}_f \cdot \nabla \mathbf{v}_f = -\nabla p + \mu \nabla^2 \mathbf{v}_f + \mathbf{S}_v, \quad (3.21)$$

where  $\mathbf{S}_v$  is a source term inserted into the momentum equation strictly for using the manufacturing solution method.

The finite volume method uses a collocated variable arrangement, and the time discretization is done using the BDF2 time scheme. Therefore, the theoretical order-of-accuracy for the spatial and temporal discretization of the velocity components is second-order, which is the order we need to observe to verify the code order-of-accuracy. In a pressure-correction coupling technique, the numerical solution for pressure matches the exact solution in variation and not in actual value, so whether the pressure matches the order of accuracy is less critical.

A coverage test suite is designed to test the accuracy of the code. I use simple manufactured solutions (Eq.#) for the three velocity components and the pressure. They have been previously used to verify other solvers for incompressible fluids (Banks, Aslam, & Rider, 2008; Cenicerros, N3s, & Roma, 2010; Choudhary et al., 2016; Vedovoto, Silveira Neto, Mura, & Figueira da Silva, 2011) since they are built in such a manner that the velocity divergence is zero.

$$\begin{aligned} u(\mathbf{x}, t) &= \sin^2(2\pi x + 2\pi y + 2\pi z + t), \\ v(\mathbf{x}, t) &= \cos^2(2\pi x + 2\pi y + 2\pi z + t), \\ w(\mathbf{x}, t) &= 1, \\ p(\mathbf{x}, t) &= \cos(2\pi x + 2\pi y + 2\pi z + t). \end{aligned} \quad (3.22)$$

The Source term  $\mathbf{S}_v$  is generated using Mathematica after substituting the manufactured solutions into the momentum equation and subsequent derivation of it. The source term is inserted in the numerical code, enabling the manufactured solution to be reproduced.

The computational domain is a cube of dimension  $[0,1] \times [0,1] \times [0,1]$ , in x, y, z directions, respectively. All the boundaries are set as inflow boundaries conditions and are prescribed by computing the manufactured solutions for these locations. The density and viscosity are set to unity. The number of corrector PRIME steps is limited to 2. The manufactured solution is evaluated to the initial time and given as an initial condition to assure that the error will tend to zero when the mesh

is refined. The iterative convergence tolerance on the residual is set to  $10^{-12}$ . The time step is constant and equal to  $10^{-4}$ , and the simulation terminates at 100 time-steps.

Six orthogonal and uniform different grids,  $8^3$ ,  $16^3$ ,  $32^3$ ,  $64^3$ ,  $128^3$ , and  $256^3$ , with a refinement ratio of two, were used in the grid convergence testing. Fig. 8 shows the computed solution of the velocity components and the pressure for the finest grid that is quite similar to the manufactured solutions.

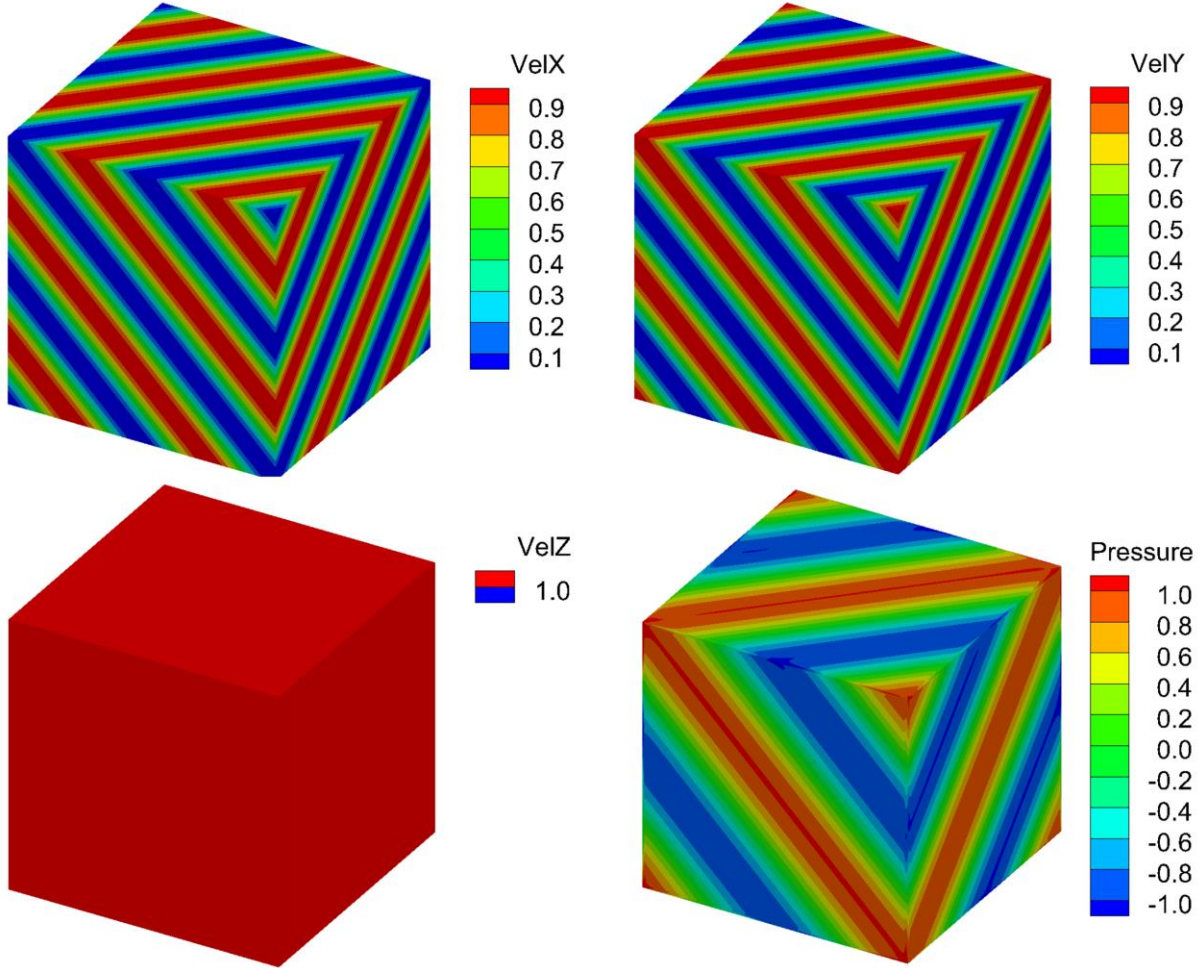


Fig. 8 The computed velocity contours on the x, y, and z-directions and the pressure contours at  $t=10^{-3}$ s (100 time-steps) using the finest grid.

For each grid, the global discretization error was determined with the  $L_2$  norm given by

$$L_2 \text{ norm} = \sqrt{\frac{\sum_n (u_n - U_n)^2 V_n}{\sum_n V_n}}, \quad (3.23)$$

where  $n$  denotes the index of the discrete solution location,  $u_n(\mathbf{x}_n, t)$  is the exact solution evaluated at  $\mathbf{x}_n, t$ , while  $U_n$  is the discrete solution at the same point in space and time, and  $V_n$  is the local volume. Then, the observed order of accuracy,  $p$ , of the code was estimated from the global error as

$$p = \frac{\ln\left(\frac{E(grid_1)}{E(grid_2)}\right)}{\ln(r)} \quad (3.24)$$

where  $E(grid_1)$  and  $E(grid_2)$  are the global discretization errors on two different grids, and  $r$  is the refinement ratio. Table 1 collects the results for the six grids, whereas Fig. 9 presents the L2 norm of the three velocity components and the pressure in a logarithmic scale for the six refinement grid levels. For a better appreciation of the order of the error decay, the theoretical second order-of-precision is included in the graph.

Table 1 Global discretization error and order of accuracy for the proposed pressure-velocity coupling for a single incompressible 3D fluid

Grid level	Domain	u		v		w		p	
		L <sub>2</sub> norm	order	L <sub>2</sub> norm	order	L <sub>2</sub> norm	order	L <sub>2</sub> norm	order
1	8 <sup>3</sup>	4.13E-2	---	4.15E-2	---	2.20E-2	---	1.23E+0	---
2	16 <sup>3</sup>	1.09E-2	1.92	1.10E-2	1.92	5.72E-3	1.95	3.62E-1	1.77
3	32 <sup>3</sup>	2.97E-3	1.88	2.97E-3	1.88	1.72E-3	1.73	1.17E-1	1.64
4	64 <sup>3</sup>	7.62E-4	1.96	7.62E-4	1.96	4.71E-4	1.87	3.56E-2	1.71
5	128 <sup>3</sup>	1.92E-4	1.99	1.92E-4	1.99	1.21E-4	1.96	1.19E-2	1.58
6	256 <sup>3</sup>	4.80E-5	2.00	4.80E-5	2.00	3.05E-5	1.99	4.21E-3	1.50

For the single 3D incompressible fluid, the alternative proposed pressure-velocity coupling has proven to achieve second-order of accuracy for velocity. For the pressure, it is possible to note a continuous decrease of the error as the computational mesh is refined. However, its order-of-accuracy fluctuates between 1.50 to 1.77.

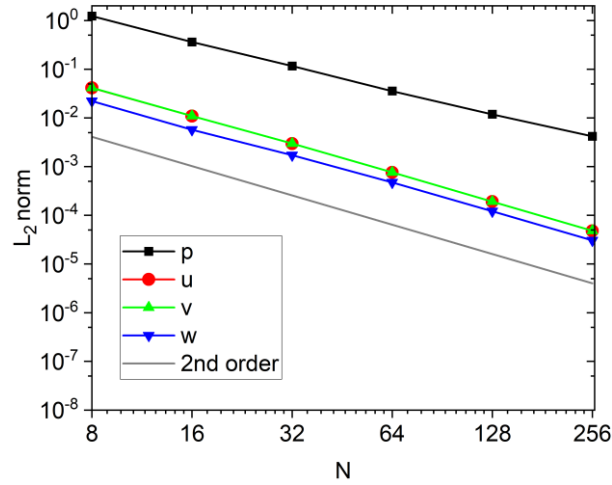


Fig. 9 L<sub>2</sub> norm of three velocity components and the pressure for the manufactured solution and the theoretical. The solid line stands for the second-order decay.

In order to check the advantages or disadvantages in the accuracy and efficiency of the new coupling algorithm, the manufactured solutions method was again applied to the original SIMPLE algorithm pre-existing in the FASTEST solver. The global discretization error for each grid level and the observed order-of-accuracy were the same values already presented in Table 1 for which reason its presentation is omitted. This similarity in the results led to confirm that the implementation of the new pressure-velocity coupling algorithm is correct. On the other hand, a significant difference in computational time was observed. Table 2 contents a comparative study of the total number of iterations and real-time required to achieve convergence for the SIMPLE algorithm with two internal PRIME loops, a) the new implementations, and for the SIMPLE algorithm, b) the standard FASTEST

implementation. The option a) requires around 60% to 80% less outer iterations than option b). In real-time, this reduction represents about 20% to 50% of calculations time for all the grid level except for the fifth domain for which seems to be more efficient to use the standard SIMPLE.

In conclusion, the best performance is observed for the coarse grids. I suppose that the Courant numbers ( $Co$ ) for coarse grids are relatively small in comparison to the finer grids which confirms that the SIMPLE algorithm is the best option for large time steps and steady-state cases as is mentioned in (F. Moukalled et al., 2016). Nevertheless, the general application of this research work, solving free-surface flows, does not require large time steps since this produces numerical dissipation. For this reason, the efficiency that offers the new pressure-velocity coupling implementation is a desirable feature and will be used for every test-case when the  $Co$  is less than one to avoid possible stability problems.

Table 2 Comparison of the total number of iterations to compute the manufactured solutions using the standard SIMPLE algorithm and the SIMPLE algorithm with two internal PRIMER loops.

Domain	$Co$	a) SIMPLE & PRIMER loop		b) SIMPLE		Performance $(1 - a/b)$	
		Iterations	Time (s)	Iterations	Time	Iterations	Real-time
$8^3$	8.51E-04	871	2.31	4318	4.48	80%	48%
$16^3$	1.64E-03	928	19.09	4604	34.23	80%	44%
$32^3$	3.22E-03	1412	57.65	8989	97.87	84%	41%
$64^3$	6.41E-03	2328	229.61	8591	326.34	73%	30%
$128^3$	1.28E-02	4004	2419.50	9824	2285.30	59%	-6%
$256^3$	2.56E-02	7465	42285.00	20058	52789.00	63%	20%

## 4.2. Validation of the fluid-structure interaction coupling

For the validation of the new fluid-structure interaction coupling approach, the FSI3 benchmark proposed by Turek and Hron (Stefan Turek & Hron, 2006) is solved. This test case was successfully simulated with various numerical approaches in (S. Turek, Hron, Razzaq, Wobker, & Schäfer, 2011) and nowadays this is a well-established standard validation test in the FSI community, e.g. (Bungartz et al., 2016; Sachs, 2012; Uekermann, 2016). The FSI3 benchmark involves an incompressible Newtonian and laminar flow interacting with an elastic bar attached to a fixed cylinder which results in self-induced oscillations of the structure. Fig. 10 shows the geometrical configuration and boundary conditions for the FSI3 test case. At the left boundary, a parabolic inflow velocity profile is prescribed, while at the right boundary, an outflow with zero gradient condition is assumed. The top and bottom of the channel and the surface of the complete structure are set as no-slip boundaries. For details about the overall setup of the interaction problem, see (Stefan Turek & Hron, 2006).

The validation is carried out by solving three grid levels with a refinement factor of 2 in the  $x$  and  $y$  direction for the fluid and solid subdomains. Once the dynamic movement of the bar converges in periodic oscillations, the mean values, amplitudes, and frequencies of the displacement of point A and the total draglift forces around the cylinder and elastic bar are compared with the reference values presented in (S. Turek et al., 2011).

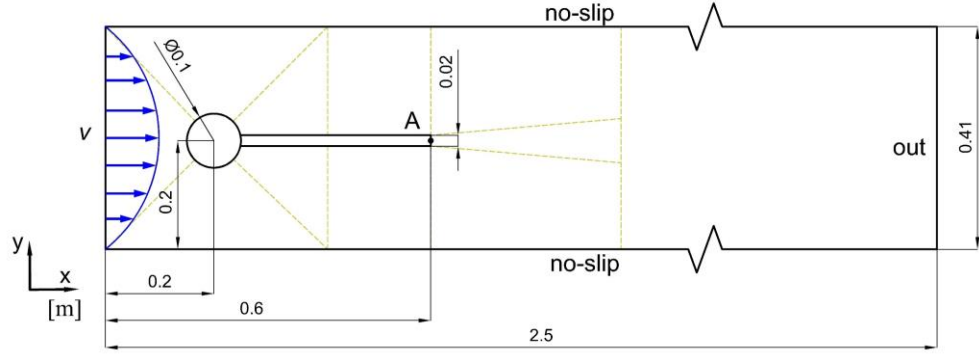


Fig. 10 The geometric configuration and boundary condition of the FSI3 benchmark test case. The dimensions are given in meters. A is the control point. The dashed lines indicate the distribution of the blocks in the fluid grid.

The fluid domain is discretized by a block-structured grid that consists of 11 blocks of hexahedral control volumes distributed as is shown with dashed lines in Fig. 10. The coarse mesh consists of 15232, the medium of 60928, and the fine of 243712 control volumes. As this case is 2D and the fluid solver, FASTEST, is a 3D solver, a quasi-two-dimensional setup is achieved by setting slip boundary conditions in the  $z$ -direction and using only a control volume of 0.01 m thickness. Furthermore, the velocity and distortion in the  $z$ -direction are set to zero. The time integration of the equations is performed with the BDF2 scheme. The internal convergence in the fluid solver, FASTEST is set to  $10^{-7}$  and limited to maximum 10 SIMPLE iterations without internal PRIME loop per each FSI iteration which in this case is enough to achieve accurate results and maintain the coupling stable. The grid remeshing is handled with the linear transfinite interpolation (TFI) method. Information about grid movement techniques and their influence in fluid-structure interaction computations can be found, for example, in (Yigit, Schäfer, & Heck, 2008).

On the other hand, the structural part is discretized by a structure grid of fully integrated linear eight-node brick elements (C3D8 element type in Calculix). The shape function is described in (Lapidus & Pinder, 1982). The number of elements for the coarse, medium, and fine mesh are  $32 \times 2$ ,  $64 \times 4$ ,  $128 \times 8$ , respectively. All nodes are limited to two degrees of freedom (translation in  $x$  and  $y$ ). The material is defined as Saint-Venant Kirchhoff material considering the nonlinear geometric calculations. The dynamic analysis is conducted with the direct integration analysis that integrates the equation of motion in time with the classical Newmark method. The convergence criteria used are the default values in Calculix.

For the FSI coupling, an implicit serial coupling is set with a constant under-relaxation of 0.2, a maximum number of FSI iterations per time step of 50, and the relative convergence threshold of  $10^{-6}$  for displacements and  $10^{-2}$  for forces. The convergence criteria were chosen after testing that a stricter convergence limit for the forces slows down the simulation too much without significantly improving the results. The time step size for the three grid levels is a constant value of  $2 \times 10^{-3}$  s for the two solvers. The grids for the fluid and structure part are no matching grids at the coupling interface, so the displacement and forces at the interface are mapped with the radial basis function method without considering the  $z$ -direction. Also, a second-order extrapolation for the displacements is applied to accelerate the calculation.

Initially, the flow is developed without the structural model until this converges to a periodic regime (16 seconds), then this solution is imposed as an initial condition for the FSI case. The simulation is run for 4 s, where the first 2 seconds show an influence of the transient phase, and the last part shows a periodic oscillations behavior. Fig. 11 shows the velocity profile in the  $x$ -direction, the coarse fluid mesh distortion, and the position of the structure at times  $t=19.7$  s and  $t=19.8$  s.



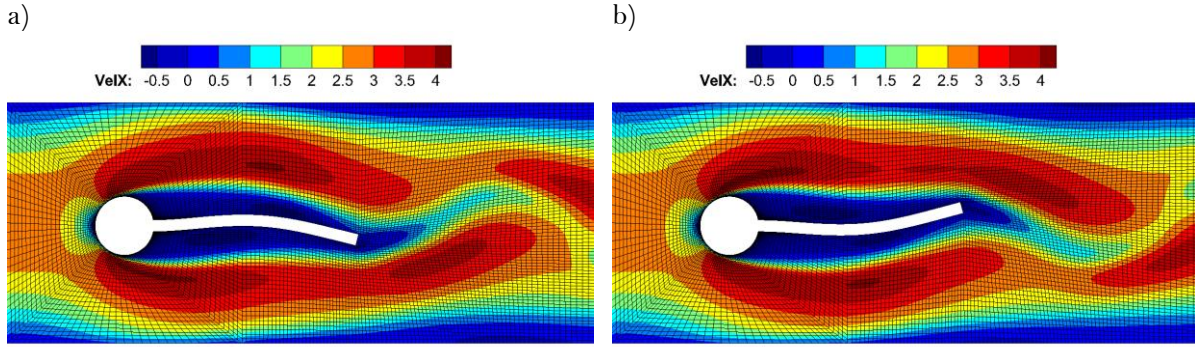


Fig. 11 x-velocity profile and coarse grid distortion for the FSI3 benchmark case for a)  $t=19.7s$  and for b)  $t=19.8s$ .

Fig. 12 displays the displacements in a) x and b) y-direction, as well as, the total c) lift and d) drag forces for the three grid levels over time from, 19.5s to 20s. The reference values are the results obtained by Turek/Hron downloaded from [http://www.featflow.de/en/benchmarks/cfdbenchmarking/fsi\\_benchmark.html](http://www.featflow.de/en/benchmarks/cfdbenchmarking/fsi_benchmark.html), while Table 3 lists the relevant benchmark values computed from the second oscillation after  $t = 19.5$  s. As reference values are taken the results obtained with two of the different methods presented in (S. Turek et al., 2011).

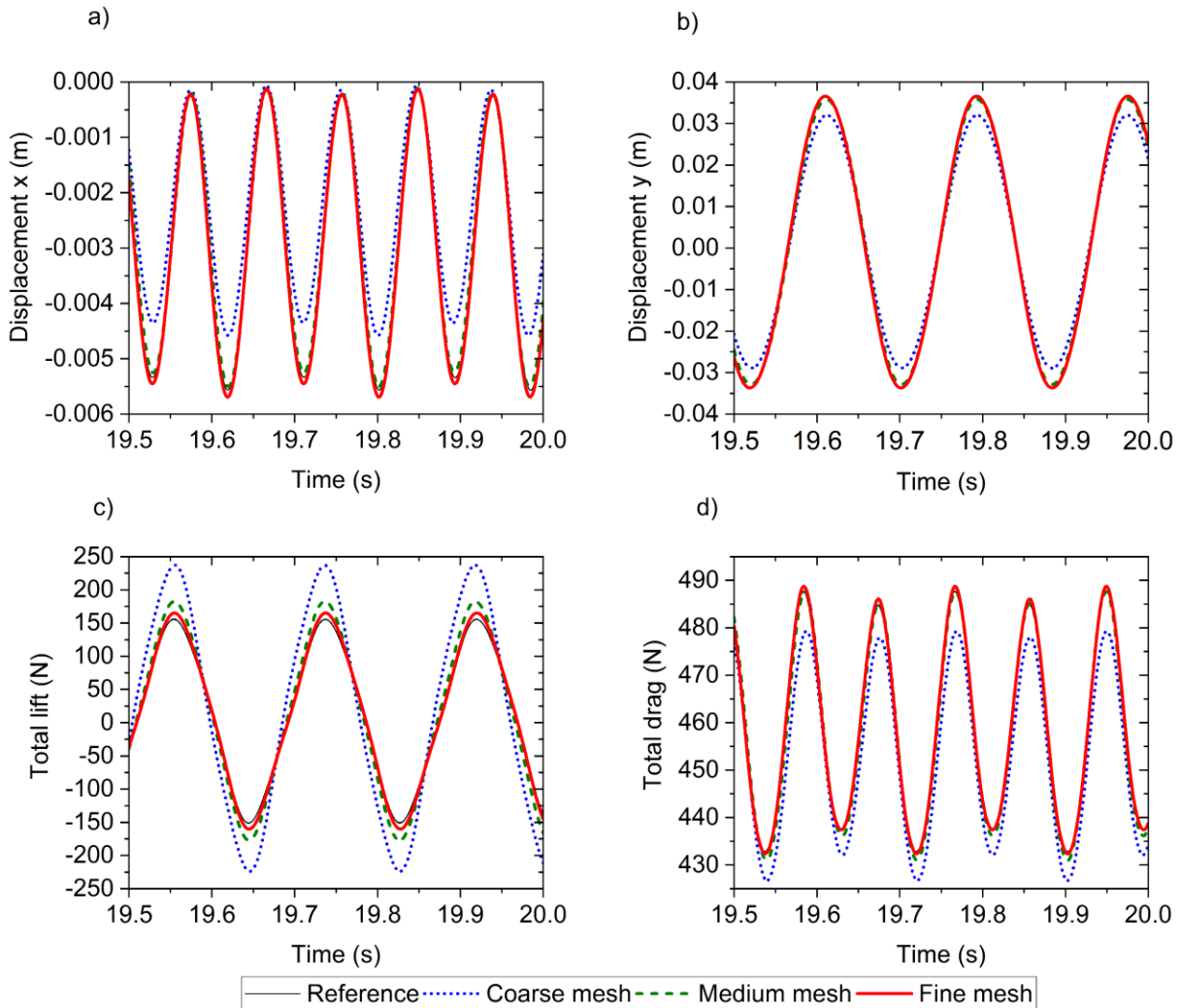


Fig. 12 Displacement and force values for the FSI3 benchmark test case for the three grids levels and the reference values download from [http://www.featflow.de/en/benchmarks/cfdbenchmarking/fsi\\_benchmark.html](http://www.featflow.de/en/benchmarks/cfdbenchmarking/fsi_benchmark.html), a) displacement of point A in x-direction, b) displacement of point A in y-direction, c) total lift forces on the cylinder with elastic bar, and d) total drag forces on the cylinder with elastic bar.



Table 3 Displacement values at point A and lift-drag forces on the cylinder with the elastic bar for the FS3 benchmark test case. The values are given as the mean  $\pm$  amplitude [frequency] and are computed from the second oscillation after  $t = 19.5$  s. The \* regards to reference values presented by Turek/Hron for the grid with 304 128 unknowns and  $\Delta t = 0.00025$  s, and Schäfer for the grid with 237 286 unknowns and  $\Delta t = 0.002$  s in (S. Turek et al., 2011).

Grid level	$u_x(A)$ [ $10^{-3}$ m]	$u_y(A)$ [ $10^{-3}$ m]	LIFT [N]	DRAG [N]
Coarse	$-2.32 \pm 2.25$ [10.75]	$1.57 \pm 30.5$ [5.68]	$6.61 \pm 230.43$ [5.56]	$453.01 \pm 26.31$ [10.87]
Medium	$-2.81 \pm 2.69$ [10.64]	$1.49 \pm 34.3$ [5.49]	$2.75 \pm 179.61$ [5.49]	$459.32 \pm 28.33$ [11.11]
Fine	$-2.91 \pm 2.78$ [10.87]	$1.48 \pm 35.1$ [5.46]	$2.60 \pm 162.59$ [5.43]	$460.58 \pm 28.19$ [10.64]
Turek/Hron*	$-2.88 \pm 2.72$ [10.93]	$1.47 \pm 35.0$ [5.46]	$2.50 \pm 153.91$ [5.46]	$460.50 \pm 27.47$ [10.93]
Schäfer*	$-2.88 \pm 2.73$ [10.60]	$1.53 \pm 34.9$ [5.30]	$2.08 \pm 153.10$ [5.30]	$458.60 \pm 27.18$ [10.60]

The coarse grid presents more discrepancy to the reference value, which is due to a too coarse spatial discretization. However, the medium and fine grid levels are close to the reference results. In general, the maximum differences between the results of the finest grid level and the reference values are around 4%, and only the mean lift force value is 25% different if we compare with the results computed by Schäfer, although this value is also 16% different from the results of Turek/Hron.

Finally, other important points of a partitioned FSI coupling algorithm are efficiency, robustness, and stability which are closely linked to the type of meshes, conforming or non-conforming meshes at the coupling interface, thus implicitly the mapping strategy, and the method used to solve the fixed-point iterations process in the coupling tool preCICE (Bungartz et al., 2016). Here, the results obtained with a constant under-relaxation of 0.2, which required around 29 FSI iterations per time step for the coarse grid, and 36 for the medium and fine grid were presented. However, several other settings in the preCICE configuration file were tested but are not shown here because they were less efficient or unstable. For instance, using the under-relaxation factor of 0.05 and increasing the number of maximum FSI iterations to 200, around 75 FSI iterations per time-step are required for the coarse and medium grid, and the fine grid becomes unstable. For a stable simulation, a smaller time step of 0.001s was used that required 126 FSI iterations per time-step. Thus, the computational time for the coarse and medium grid levels was doubled and quadrupled for the finest grid level, although the convergence criterium for the displacement was reduced to  $10^{-4}$ .

In summary, the validation test case, the FS3 benchmark, was successful simulated using the new proposed FSI coupling algorithm. The displacement and forces agree with the reference results. Consequently, the algorithm works properly and can be used for other FSI test cases. Concerning efficiency and stability, several parameters can be tested in the coupling tool. Nevertheless, it was not the objective of this validation analysis. The reader can find other ideas to solve this test case, e.g. in (Gillebaart et al., 2016) or (Mehl et al., 2016) where used matching grids at the FSI interface, and the quasi-Newton methods to accelerate the fixed-point iteration reducing the computational time considerably.